



A numerical model for three-dimensional shallow water flows with sharp gradients over mobile topography

Xin Liu*, Abdolmajid Mohammadian, Julio Ángel Infante Sedano

Department of Civil Engineering, University of Ottawa, 161 Louis Pasteur St., Ottawa, Canada



ARTICLE INFO

Article history:

Received 17 April 2016

Revised 15 May 2017

Accepted 22 May 2017

Available online 23 May 2017

Keywords:

3-D shallow water equations

σ -coordinates

Relaxation method

Bed erosion

Finite volume method

Dam-break

ABSTRACT

This study aims to develop a three-dimensional (3-D) numerical model for shallow water flows over mobile topography, which is capable of simulating morphological evolution under shock waves, e.g. dam-break flows. The hydrodynamic model solves the three-dimensional shallow water equations (SWEs) using a finite volume method on prismatic cells in σ -coordinates. The morphodynamic model solves an Exner equation consisting of bed-load sediment transportation. Using a relaxation approach, a hyperbolic system is built for hydrodynamic system, which allows for using a Godunov-type central-upwind method to capture the shocks and approximate the numerical fluxes. Consequently, the 3D-SWEs-Exner model proposed in the present study can stably and accurately solve the dam-break flows over mobile beds. A spatially and temporally second-order “prismatic” central-upwind method is used to approximate the numerical fluxes through cell interfaces. The Exner equation is solved using an upwind method. Using spatially linear reconstruction and explicit two-stage Runge-Kutta time discretization, second order accuracy is achieved in space and time. The proposed model can preserve the well-balanced property due to the special discretization of bed-slope source terms. The proposed model is validated by several tests with experimental measurements, and is compared with the simulated results using reported two-dimensional (2-D) models.

© 2017 Elsevier Ltd. All rights reserved.

1. Introduction

In the past few decades, a number of 2-D numerical models for shallow water (SW) flows with shocks over mobile topography have been developed based on 2-D depth-averaged SWEs. Vásquez [39] have developed a 2-D river morphology model referred as River2D-MOR which has been tested for dam-break flows over mobile bed in [38]. Zhang and Wu have developed a 2-D hydrodynamic and sediment transport model for dam break flows using finite volume method based on quad-tree grids [42]. Xia et al. [41] have developed a 2-D numerical model for dam-break flows over mobile bed using a coupled approach. Evangelista et al. [7] proposed a 2-D model to simulate dam-break waves on movable beds using a multi-stage centered scheme. Swartenbroekx et al. [36] have built a 2-D two-layer shallow water model for dam break flows with significant bed load transport. Liu et al. [22] developed a robust 2-D model for rapidly varying flows over erodible bed with wetting and drying. Canelas et al. [6] proposed a novel two-dimensional depth-averaged simulation tool for highly

unsteady discontinuous flows over complex time-evolving geometries. Liu et al. [24] developed a well-balanced 2-D coupled model for dam-break flow over erodible bed. Wei et al. [11] have conducted a 2D hydrodynamic and sediment transport modeling of mega flood due to dam-break. Liu et al. [21] have proposed a two dimensional numerical model for rapidly varying flow over mobile bed, which is suitable for dam-break cases.

There are only a limited number of studies of 3-D shallow water models over erodible beds. Lesser et al. [20] discussed the operation of the DELFT3D module and presented the key features of the formulations used to model the fluid flow and sediment transport over mobile bed, in which the hydrodynamic module solves the 3-D shallow water equations [3,4] based on assumption of hydrostatic status, using the finite difference method. However, the numerical model proposed in [20] cannot guarantee shock-capturing ability, therefore, it may fail in simulations of bed-erosion under unsteady-flows with sharp gradients, e.g., dam-break flows. This prevents the extension of this model to the cases with shocks waves.

Inspired by the study [20], in this study, a 3-D numerical model is developed using the 3-D SWEs and Exner formula. Unlike the previously reported 3-D SW model over mobile bed [20] which may fail in solving sharp gradients, the proposed model can stably

* Corresponding author.

E-mail addresses: xliu11@uottawa.ca, liuxin429go@gmail.com (X. Liu).

simulate the bed evolution under dam break waves. This is accomplished by converting the 3-D SWEs into a hyperbolic form using a relaxation approach based on the work [1,23], which allows for the use of shock capturing schemes, e.g. central-upwind method. Consequently, the model is able to simulate dam-break flows without numerical instability. Furthermore, a second order “prismatic” central-upwind method is used to estimate the fluxes through interfaces based on explicit finite volume method. The temporal evolution of topography is estimated by an Exner equation consisting of bed-load transport which is estimated by an upwind method. A stable total variation diminishing two-stage Runge-Kutta (TV-DRK2) solver is used in the proposed model to gain second order temporal accuracy. The model is validated by several laboratory tests with experimental data; the proposed 3-D model is compared with several reported 2-D models; and the simulated results using depth-averaged velocities are also compared with those using near bed velocities.

2. Governing equations

2.1. Hydrodynamic model

3-D SWEs with constant density are derived from the 3-D Navier-Stokes equations, after Reynolds-averaging and under the simplifying assumptions of hydrostatic pressure (see [3,4]). Ignoring the horizontal viscous terms and coriolis effect, the 3-D SWEs have the following form:

$$\frac{\partial u}{\partial x} + \frac{\partial v}{\partial y} + \frac{\partial w}{\partial z} = 0 \quad (1)$$

$$\frac{\partial u}{\partial t} + \frac{\partial uu}{\partial x} + \frac{\partial vu}{\partial y} + \frac{\partial wu}{\partial z} = \frac{\partial}{\partial z} \left(v_w \frac{\partial u}{\partial z} \right) - g \frac{\partial \eta}{\partial x} \quad (2)$$

$$\frac{\partial v}{\partial t} + \frac{\partial uv}{\partial x} + \frac{\partial vv}{\partial y} + \frac{\partial ww}{\partial z} = \frac{\partial}{\partial z} \left(v_w \frac{\partial v}{\partial z} \right) - g \frac{\partial \eta}{\partial y} \quad (3)$$

where t is the time; x , y and z are the Cartesian coordinates; $u(x, y, z, t)$, $v(x, y, z, t)$ and $w(x, y, z, t)$ are the velocity components in the x -, y - and z -directions, respectively; g is the gravitational acceleration; $\eta(x, y, t)$ is the water surface elevation; and v_w is the kinematic vertical eddy viscosity. The system (1)–(3) together with either kinematic or dynamic boundary conditions for η constitute a closed system of equations for u , v , w and η .

In order to more accurately define the irregularly bottom boundary, the σ coordinate is adopted in the vertical direction to replace the Cartesian coordinate z using the following transformation [3,4,28]:

$$\sigma = \frac{z - \eta(x, y, t)}{D(x, y, t)} = \frac{z - \eta(x, y, t)}{\eta(x, y, t) - h(x, y, t)}, \quad (4)$$

where σ is the transformed vertical coordinate that varies between -1 and 0 , $D(x, y, t)$ is the depth of the water column, and $h(x, y, t)$ is the bed level.

Accordingly, the 3-D SWEs in σ -coordinates can be written in the following form:

$$\frac{\partial \eta}{\partial t} + \frac{\partial (Du)}{\partial x} + \frac{\partial (Dv)}{\partial y} + \frac{\partial \omega}{\partial \sigma} = 0 \quad (5)$$

$$\begin{aligned} \frac{\partial (Du)}{\partial t} + \frac{\partial}{\partial x} \left(Du^2 + \frac{g}{2} D^2 \right) + \frac{\partial (Dvu)}{\partial y} + \frac{\partial (\omega u)}{\partial \sigma} \\ = \frac{\partial}{\partial \sigma} \left(v_w \frac{\partial u}{\partial \sigma} \right) - g D \frac{\partial h}{\partial x} \end{aligned} \quad (6)$$

$$\frac{\partial (Dv)}{\partial t} + \frac{\partial (Duv)}{\partial x} + \frac{\partial}{\partial y} \left(Dv^2 + \frac{g}{2} D^2 \right) + \frac{\partial (\omega v)}{\partial \sigma}$$

$$= \frac{\partial}{\partial \sigma} \left(\frac{v_w}{D} \frac{\partial v}{\partial \sigma} \right) - g D \frac{\partial h}{\partial y} \quad (7)$$

where ω is the vertical velocity in the σ -direction, which is related to w by the following relationship:

$$\omega = w - u \left(\sigma \frac{\partial D}{\partial x} + \frac{\partial \eta}{\partial x} \right) - v \left(\sigma \frac{\partial D}{\partial y} + \frac{\partial \eta}{\partial y} \right) - \left(\sigma \frac{\partial D}{\partial t} + \frac{\partial \eta}{\partial t} \right). \quad (8)$$

We apply the kinematic boundary condition $\omega(x, y, \sigma = -1, t) = 0$ and $\omega(x, y, \sigma = 0, t) = 0$ to close the system (5)–(7). Integrating the continuity Eq. (5) with respect to σ from -1 to 0 using Leibniz's rule gives the following free surface equation:

$$\frac{\partial \eta}{\partial t} + \frac{\partial}{\partial x} \left[\int_{-1}^0 Du d\sigma \right] + \frac{\partial}{\partial y} \left[\int_{-1}^0 Dv d\sigma \right] = 0. \quad (9)$$

The vertical eddy viscosity can be estimated by the following model [29] in σ -coordinates:

$$v_w = \left(\frac{\ell_m}{D} \right)^2 \left[\left(\frac{\partial u}{\partial \sigma} \right)^2 + \left(\frac{\partial v}{\partial \sigma} \right)^2 \right]^{1/2} \quad (10)$$

where ℓ_m is the mixing length which can be approximated by:

$$\ell_m = \begin{cases} \kappa(\sigma + 1)D, & \text{if } \sigma \leq -0.75, \\ 0.1D, & \text{otherwise.} \end{cases} \quad (11)$$

where $\kappa = 0.41$ is the Von Karman constant.

2.2. Morphodynamic model

In the current study, the topography is evaluated by the Exner equation,

$$\frac{\partial h}{\partial t} + \xi \frac{\partial q_{b,x}}{\partial x} + \xi \frac{\partial q_{b,y}}{\partial y} = 0 \quad (12)$$

in which ξ is a coefficient equal to $(1 - p)^{-1}$; p is the bed porosity; and $q_{b,x}$ and $q_{b,y}$ are components of bed-load discharge q_b in x and y -directions, respectively.

In this study, the bed-load transport rate is estimated by the Meyer-Peter and Müller (MPM) formula [25],

$$q_b = C_B \sqrt{(s - 1)gd^3} \cdot (\theta - \theta'_c)^3 \quad (13)$$

in which C_B is the bed-load coefficient; s is the specific gravity of sediment given by $s = \rho_s/\rho_f$, where ρ_s is the density of sediment particles and ρ_f is the density of water; d is the mean particle diameter; θ'_c is modified critical bed shear stress, θ_c is the critical bed shear stress that can be estimated by the following formula [35]

$$\theta_c = \frac{0.3}{1 + 1.2d^*} + 0.055(1 - e^{-0.02d^*}) \quad (14)$$

where d^* is the dimensionless grain size calculated by

$$d^* = d \left[\frac{g(s - 1)}{v_f^2} \right]^{1/3} \quad (15)$$

where v_f is the kinematic viscosity of fluid, and $v_f = 1 \times 10^{-6}$ m²/s is used in all the tests in this study. Considering the slope effect, θ_c estimated by (14) can be modified using [34]

$$\theta'_c = \theta_c \frac{\cos \psi \sin \beta + \sqrt{\cos^2 \beta \tan^2 \phi - \sin^2 \psi \sin^2 \beta}}{\tan \phi} \quad (16)$$

where $\phi = 30^\circ$ is the angle of repose of the bed material (sand) used in the current study, β is the angle of the bed and ψ is the angle between the upslope direction of the sloping bed and the direction of the flow.

The dimensionless bed shear stress, θ , can be calculated as

$$\theta = \frac{\tau_b}{[gd(\rho_s - \rho_f)]} \quad (17)$$

in which the bed shear stress τ_b normal to the cell interface is determined as

$$\begin{aligned} \tau_b &= \tau_{b,x}n_x + \tau_{b,y}n_y, & \tau_{b,x} &= \rho_f C_d u_0 \sqrt{u_0^2 + v_0^2} \quad \text{and} \\ \tau_{b,y} &= \rho_f C_d v_0 \sqrt{u_0^2 + v_0^2} \end{aligned} \quad (18)$$

where n_x and n_y are components of unit normal vector \mathbf{n} in the x and y directions, respectively; $\tau_{b,x}$ and $\tau_{b,y}$ are the horizontal components of τ_b in the x and y directions, respectively; u_0 and v_0 are the near bed velocities estimated in the bottom layer of the computational grids; and C_d is the drag coefficient that can be locally determined in terms of the Nikuradse roughness k_s [35],

$$C_d = \left[\frac{\kappa}{0.71 + \ln\left(\frac{k_s/30}{D}\right)} \right]^2 \quad (19)$$

where k_s is estimated by $k_s = C_N d$ in which C_N is the coefficient that is set to 3.5 in this study.

Substituting Eq. (18) into Eq. (17) gives

$$\theta = \frac{C_d}{gd(s-1)(\eta-h)^2} [(Du)_0 n_x + (Dv)_0 n_y] \sqrt{(Du)_0^2 + (Dv)_0^2} \quad (20)$$

in which $(Du)_0$ and $(Dv)_0$ are the horizontal discharge components in the bottom layer of computational grids. Accordingly, the dimensionless shear stress θ used in (13) can be estimated by bottom flow discharges $(Du)_0$ and $(Dv)_0$ using (20) in this study.

3. A relaxation system of hydrodynamic model

Since the governing system (5)–(7) is not in a hyperbolic form, one can not apply a shock capturing solver on the system. Consequently, the shock-capturing ability of the numerical method cannot be guaranteed. In order to stably and accurately simulate the sharp gradient and discontinuities in 3-D shallow water flows, in the present study, a relaxation model of the 3-D SWEs is built using the approach given in [1,23], which is hyperbolic and equivalent to the original model in the zero relaxation limit ($\varepsilon \rightarrow 0^+$). In order to obtain the relaxation model, an auxiliary variables ω' is introduced to replace the variable ω , and a partial differential equation with a stiff source term is added to the original system, which lead to the following relaxation system

$$\frac{\partial \eta}{\partial t} + \frac{\partial (Du)}{\partial x} + \frac{\partial (Dv)}{\partial y} + \frac{\partial \omega'}{\partial \sigma} = 0 \quad (21)$$

$$\begin{aligned} \frac{\partial (Du)}{\partial t} + \frac{\partial}{\partial x} \left(Du^2 + \frac{gD^2}{2} \right) + \frac{\partial (Dvu)}{\partial y} + \frac{\partial (\omega' u)}{\partial \sigma} \\ = \frac{\partial}{\partial \sigma} \left(\frac{v_v}{D} \frac{\partial u}{\partial \sigma} \right) - Dg \frac{\partial h}{\partial x} \end{aligned} \quad (22)$$

$$\begin{aligned} \frac{\partial (Dv)}{\partial t} + \frac{\partial (Duv)}{\partial x} + \frac{\partial}{\partial y} \left(Dv^2 + \frac{gD^2}{2} \right) + \frac{\partial (\omega' v)}{\partial \sigma} \\ = \frac{\partial}{\partial \sigma} \left(\frac{v_v}{D} \frac{\partial v}{\partial \sigma} \right) - Dg \frac{\partial h}{\partial y} \end{aligned} \quad (23)$$

$$\frac{\partial \omega'}{\partial t} + W^* \frac{\partial \omega'}{\partial \sigma} = -\frac{1}{\varepsilon} (\omega' - \omega) \quad (24)$$

where $\varepsilon > 0$ is a relaxation parameter and W^* is a very small propagation speed associated with the auxiliary variable ω' (in all of

the numerical tests, $W^* = 10^{-8}$ is used to avoid additional stability restriction, see [23]).

The system (21)–(24) can be written in the following vector form:

$$\mathbf{U}_t + \mathbf{F}(\mathbf{U}, h)_x + \mathbf{G}(\mathbf{U}, h)_y + \mathbf{K}(\mathbf{U}, h)_\sigma = \mathbf{S}(\mathbf{U}, h) + \mathbf{P}(\mathbf{U}) + \mathbf{R}(\mathbf{U}) \quad (25)$$

where $\mathbf{U} := (\eta, Du, Dv, \omega')^\top$; \mathbf{F} , \mathbf{G} and \mathbf{K} are the fluxes:

$$\mathbf{F}(\mathbf{U}, h) := \left(Du, \frac{(Du)^2}{\eta-h} + \frac{g}{2}(\eta-h)^2, \frac{(Du)(Dv)}{\eta-h}, 0 \right)^\top \quad (26)$$

$$\mathbf{G}(\mathbf{U}, h) := \left(Dv, \frac{(Du)(Dv)}{\eta-h}, \frac{(Dv)^2}{\eta-h} + \frac{g}{2}(\eta-h)^2, 0 \right)^\top \quad (27)$$

$$\mathbf{K}(\mathbf{U}, h) := \left(\omega', \frac{(Du)\omega'}{\eta-h}, \frac{(Dv)\omega'}{\eta-h}, W^*\omega' \right)^\top \quad (28)$$

and \mathbf{S} , \mathbf{P} and \mathbf{R} are the source terms:

$$\mathbf{S}(\mathbf{U}, h) := \left(0, -(\eta-h)g \frac{\partial h}{\partial x}, -(\eta-h)g \frac{\partial h}{\partial y}, 0 \right)^\top \quad (29)$$

$$\mathbf{P}(\mathbf{U}) := \left(0, \frac{\partial}{\partial \sigma} \left(\frac{v_v}{D} \frac{\partial u}{\partial \sigma} \right), \frac{\partial}{\partial \sigma} \left(\frac{v_v}{D} \frac{\partial v}{\partial \sigma} \right), 0 \right)^\top \quad (30)$$

$$\mathbf{R}(\mathbf{U}) := \left(0, 0, 0, -\frac{1}{\varepsilon} (\omega' - \omega) \right)^\top \quad (31)$$

In the coupling model, the relaxation system (21)–(24) can be written in the following quasi-linear form:

$$\mathbf{U}_t + A_n(\mathbf{U}, h)\mathbf{U}_x + B_n(\mathbf{U}, h)\mathbf{U}_y + C_n(\mathbf{U}, h)\mathbf{U}_\sigma = \mathbf{S}(\mathbf{U}, h) + \mathbf{P}(\mathbf{U}) + \mathbf{R}(\mathbf{U}),$$

where the matrices $A_n := \frac{\partial \mathbf{F}}{\partial \mathbf{U}}$, $B_n := \frac{\partial \mathbf{G}}{\partial \mathbf{U}}$ and $C_n := \frac{\partial \mathbf{K}}{\partial \mathbf{U}}$. The Jacobian matrices $J_n = A_n n_x + B_n n_y$ for horizontal convection and C_n for vertical convection can be computed as

$$J_n = \begin{pmatrix} 0 & n_x & n_y & 0 \\ -\frac{(Du)q^\perp}{(\eta-h)^2} + g(\eta-h)n_x & \frac{q^\perp}{\eta-h} + \frac{Du}{\eta-h}n_x & \frac{(Du)}{\eta-h}n_y & 0 \\ -\frac{(Dv)q^\perp}{(\eta-h)^2} + g(\eta-h)n_y & \frac{(Dv)}{\eta-h}n_x & \frac{q^\perp}{\eta-h} + \frac{Dv}{\eta-h}n_y & 0 \\ 0 & 0 & 0 & 0 \end{pmatrix} \quad (32)$$

and

$$C_n = \begin{pmatrix} 0 & 0 & 0 & 1 \\ -\frac{(Du)\omega'}{(\eta-h)^2} & \frac{\omega'}{\eta-h} & 0 & \frac{Du}{\eta-h} \\ -\frac{(Dv)\omega'}{(\eta-h)^2} & 0 & \frac{\omega'}{\eta-h} & \frac{Dv}{\eta-h} \\ 0 & 0 & 0 & W^* \end{pmatrix}, \quad (33)$$

in which $q^\perp = (Du)n_x + (Dv)n_y$.

The eigenvalues of J_n and C_n are given by

$$\begin{aligned} \lambda(J_n) &= \left\{ \frac{q^\perp}{(\eta-h)} + \sqrt{g(\eta-h)}, \frac{q^\perp}{(\eta-h)}, \frac{q^\perp}{(\eta-h)} - \sqrt{g(\eta-h)}, 0 \right\} \\ \lambda(C_n) &= \left\{ \frac{\omega'}{\eta-h}, \frac{\omega'}{\eta-h}, 0, W^* \right\}. \end{aligned} \quad (34)$$

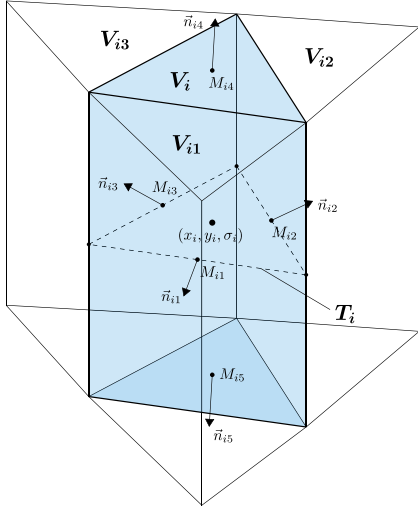


Fig. 1. A typical prismatic cell in σ coordinates.

4. Numerical algorithms for solving the 3-D SW+Exner system

Although the constructed relaxation system (21)–(24) is hyperbolic, one can not directly solve it to update all the flow parameters since η is independent on the coordinate σ . Therefore, the relaxation system (21)–(24) is solved in two steps, i.e., propagation step and relaxation step. A strang splitting method is used in the current study.

4.1. Propagation step

4.1.1. Updating the discharge components D_u and D_v

In this step, a semi-discrete second-order central-upwind scheme on prismatic grid is used. We use the 2-D triangulation coupled with the uniform grid in the σ -direction with the grid size $\Delta\sigma$. Fig. 1 shows a typical triangular prismatic cell V_i in σ coordinates, with the centroid (x_i, y_i, σ_i) and of volume $|V_i|$. The prismatic cell has five faces of areas A_{ik} , $k = 1, \dots, 5$, whose corresponding outer unit normals are denoted by $\mathbf{n}_{ik} := (n_{x,ik}, n_{y,ik}, 0)^T$, $k = 1, 2, 3$, $\mathbf{n}_{i4} := (0, 0, 1)^T$ and $\mathbf{n}_{i5} := (0, 0, -1)^T$, see Fig. 1. The corresponding neighboring cell shares the k -th face of the cell V_i is denoted by V_{ik} , $k = 1, \dots, 5$. The center of the k -th face of the cell V_i is denoted by $M_{ik} = (x_{ik}, y_{ik}, \sigma_{ik})$, $k = 1, \dots, 5$. T_i is the triangular horizontal cross-section of the prism V_i ; ℓ_{ik} , $k = 1, 2, 3$ are the lengths of the corresponding sides of the triangle T_i .

The second-order central-upwind schemes originally proposed for triangular grids [5,17] and Cartesian grids [15,16,18] are extended to a prismatic cell in this paper as

$$\begin{aligned} \frac{d\bar{\mathbf{U}}_i}{dt} = & -\frac{1}{|V_i|} \sum_{k=1}^3 \frac{A_{ik} n_{x,ik}}{a_{ik}^{\text{in}} + a_{ik}^{\text{out}}} [\bar{a}_{ik}^{\text{in}} \mathbf{F}(\mathbf{U}_{ik}(M_{ik})) + \bar{a}_{ik}^{\text{out}} \mathbf{F}(\mathbf{U}_i(M_{ik}))] \\ & -\frac{1}{|V_i|} \sum_{k=1}^3 \frac{A_{ik} n_{y,ik}}{a_{ik}^{\text{in}} + a_{ik}^{\text{out}}} [\bar{a}_{ik}^{\text{in}} \mathbf{G}(\mathbf{U}_{ik}(M_{ik})) + \bar{a}_{ik}^{\text{out}} \mathbf{G}(\mathbf{U}_i(M_{ik}))] \\ & + \frac{1}{|V_i|} \sum_{k=1}^3 A_{ik} \frac{\bar{a}_{ik}^{\text{in}} \bar{a}_{ik}^{\text{out}}}{\bar{a}_{ik}^{\text{in}} + \bar{a}_{ik}^{\text{out}}} [\mathbf{U}_{ik}(M_{ik}) - \mathbf{U}_i(M_{ik})] \\ & -\frac{1}{|V_i|} \sum_{k=4}^5 \frac{A_{ik} (-1)^k}{b_{ik}^{\text{in}} + b_{ik}^{\text{out}}} [b_{ik}^{\text{in}} \mathbf{K}(\mathbf{U}_{ik}(M_{ik})) + b_{ik}^{\text{out}} \mathbf{K}(\mathbf{U}_i(M_{ik}))] \\ & + \frac{1}{|V_i|} \sum_{k=4}^5 A_{ik} \frac{b_{ik}^{\text{in}} b_{ik}^{\text{out}}}{b_{ik}^{\text{in}} + b_{ik}^{\text{out}}} [\mathbf{U}_{ik}(M_{ik}) - \mathbf{U}_i(M_{ik})] + \bar{\mathbf{s}}_i + \bar{\mathbf{P}}_i \quad (35) \end{aligned}$$

where $\mathbf{U}_i(M_{ik})$ and $\mathbf{U}_{ik}(M_{ik})$ are the reconstructed values at M_{ik} , $k = 1, 2, 3, 4, 5$, which are obtained using a piecewise linear reconstruction,

$$\tilde{\mathbf{U}}(x, y, \sigma) := \bar{\mathbf{U}}_i + (\hat{\mathbf{U}}_x)_i(x - x_i) + (\hat{\mathbf{U}}_y)_i(y - y_i) + (\hat{\mathbf{U}}_\sigma)_i(\sigma - \sigma_i), \quad (x, y, \sigma) \in V_i, \quad (36)$$

namely,

$$\mathbf{U}_i(M_{ik}) := \lim_{\substack{(x,y,\sigma) \rightarrow M_{ik} \\ (x,y,\sigma) \in V_i}} \tilde{\mathbf{U}}(x, y, \sigma), \quad \mathbf{U}_{ik}(M_{ik}) := \lim_{\substack{(x,y,\sigma) \rightarrow M_{ik} \\ (x,y,\sigma) \in V_{ik}}} \tilde{\mathbf{U}}(x, y, \sigma). \quad (37)$$

The slopes in linear reconstruction Eq. (36) have to be limited to suppress potential nonphysical oscillations near discontinuities. In the current study, the horizontal limited slopes $\hat{\mathbf{U}}_x$ and $\hat{\mathbf{U}}_y$ are computed using a multidimensional slope limiter proposed in [13]; the vertical limited slope $\hat{\mathbf{U}}_\sigma$ is computed using the minmod limiter (see, e.g., [26,30,37]).

The horizontal directional local speeds of propagation, a_{ik}^{in} and a_{ik}^{out} , are defined by

$$\begin{aligned} a_{ik}^{\text{in}} &:= -\min \{\lambda_1[\mathbf{J}_n(U_i(M_{ik}))], \lambda_1[\mathbf{J}_n(U_{ik}(M_{ik}))], 0\} \quad k = 1, 2, 3, \\ a_{ik}^{\text{out}} &:= \max \{\lambda_n[\mathbf{J}_n(U_i(M_{ik}))], \lambda_n[\mathbf{J}_n(U_{ik}(M_{ik}))], 0\} \end{aligned} \quad (38)$$

where $\lambda_1[\mathbf{J}_n] \leq \lambda_2[\mathbf{J}_n] \leq \dots \leq \lambda_{n-1}[\mathbf{J}_n] \leq \lambda_n[\mathbf{J}_n]$ are the eigenvalues of the Jacobian matrix \mathbf{J}_n .

Similarly, the vertical directional local speeds of propagation, b_{ik}^{in} and b_{ik}^{out} , are defined by

$$\begin{aligned} b_{ik}^{\text{in}} &:= -\min \{\lambda_1[\mathbf{C}_n(U_i(M_{ik}))], \lambda_1[\mathbf{C}_n(U_{ik}(M_{ik}))], 0\}, \quad k = 4, 5, \\ b_{ik}^{\text{out}} &:= \max \{\lambda_4[\mathbf{C}_n(U_i(M_{ik}))], \lambda_4[\mathbf{C}_n(U_{ik}(M_{ik}))], 0\}, \end{aligned} \quad (39)$$

where $\lambda_1[\mathbf{C}_n] \leq \lambda_2[\mathbf{C}_n] \leq \dots \leq \lambda_{n-1}[\mathbf{C}_n] \leq \lambda_n[\mathbf{C}_n]$ are the eigenvalues of the Jacobian matrix \mathbf{C}_n .

In order to avoid division by 0 (or close to 0), in all the reported experiments, when $a_{ik}^{\text{in}} + a_{ik}^{\text{out}} < 10^{-6}$, the central-upwind method for the horizontal fluxes (first three terms on the RHS of (35)) are replaced by a Lax-Friedrichs method; when $b_{ik}^{\text{in}} + b_{ik}^{\text{out}} < 10^{-6}$, the central-upwind method for the vertical fluxes (fourth and fifth terms on the RHS of (35)) are replaced by a Lax-Friedrichs method.

Due to the discontinuity of the mobile bed at cell interfaces in this study, the discretization of the bed slope term $\bar{\mathbf{s}}_i$ in [23] can not be directly applied to the current system. Therefore, we modify the well-balanced numerical scheme in [23] and propose the following quadratures for the cell average $\bar{\mathbf{s}}_i = (0, \bar{s}_i^{(2)}, \bar{s}_i^{(3)}, 0)^T$:

$$\begin{aligned} \bar{s}_i^{(2)} = & \frac{g}{2|V_i|} \sum_{k=1}^3 A_{ik} n_{x,ik} \left[\frac{\eta_i(M_{ik}) + \eta_{ik}(M_{ik})}{2} - \frac{\bar{h}_i + \bar{h}_{ik}}{2} \right]^2 \\ & - g(\eta_x)_i (\bar{\eta}_i - \bar{h}_i), \end{aligned} \quad (40)$$

$$\begin{aligned} \bar{s}_i^{(3)} = & \frac{g}{2|V_i|} \sum_{k=1}^3 A_{ik} n_{y,ik} \left[\frac{\eta_i(M_{ik}) + \eta_{ik}(M_{ik})}{2} - \frac{\bar{h}_i + \bar{h}_{ik}}{2} \right]^2 \\ & - g(\eta_y)_i (\bar{\eta}_i - \bar{h}_i), \end{aligned} \quad (41)$$

where $(\eta_x)_i$ and $(\eta_y)_i$ are the x - and y -slope of the i th piece of the piecewise linear reconstruction of η . The well-balanced discretization (40) and (41) of the bed slope terms can preserve the “lake at rest” steady state ($\eta = \text{Constant}$, $u \equiv v \equiv \Omega \equiv 0$).

The vertical diffusion terms $\bar{\mathbf{P}}_i$ are approximated explicitly in the flux form using centered differences. At the top of the computational domain, the centered-difference approximations are re-

placed with the one-sided ones. At the bottom of the computational domain, a logarithmic velocity profile within the bottom layer is assumed [8], hence the bed shear stress is related to the turbulent law of the wall. Accordingly, we replace the vertical gradients $v_v(\partial u/\partial \sigma)$ and $v_v(\partial v/\partial \sigma)$ with $\tau_{b,x}/\rho$ and $\tau_{b,y}/\rho$ at the bottom of the computational domain.

4.1.2. Updating the water surface level η

After solving the horizontal discharges in section 4.1, we apply the kinematic boundary condition $\omega(x, y, \sigma = -1, t) = 0$ and $\omega(x, y, \sigma = 0, t) = 0$ to Eq. (9) and get

$$\frac{\partial \eta}{\partial t} + \frac{\partial}{\partial x} (\mathring{D}u) + \frac{\partial}{\partial y} (\mathring{D}v) = 0. \quad (42)$$

where $\mathring{D}u$ and $\mathring{D}v$ are depth-averaged fluxes calculated using the results from Section 4.1. Eq. (42) can be discretized in the following semi-discrete form using the "triangular" central-upwind method [5]:

$$\begin{aligned} \frac{d \bar{\eta}_i}{dt} = & - \frac{1}{|T_i|} \sum_{k=1}^3 \frac{\ell_{ik} \cos(\theta_{ik})}{a_{ik}^{\text{in}} + a_{ik}^{\text{out}}} \left[a_{ik}^{\text{in}} ((\mathring{D}u)_{ik}(M_{ik})) + a_{ik}^{\text{out}} ((\mathring{D}u)_i(M_{ik})) \right] \\ & - \frac{1}{|T_i|} \sum_{k=1}^3 \frac{\ell_{ik} \sin(\theta_{ik})}{a_{ik}^{\text{in}} + a_{ik}^{\text{out}}} \left[a_{ik}^{\text{in}} ((\mathring{D}v)_{ik}(M_{ik})) + a_{ik}^{\text{out}} ((\mathring{D}v)_i(M_{ik})) \right] \\ & + \frac{1}{|T_i|} \sum_{k=1}^3 \ell_{ik} \frac{a_{ik}^{\text{in}} a_{ik}^{\text{out}}}{a_{ik}^{\text{in}} + a_{ik}^{\text{out}}} \left[\eta_{ik}(M_{ik}) - \eta_i(M_{ik}) \right]. \end{aligned} \quad (43)$$

4.1.3. Updating the vertical velocity ω

In this step, the vertical velocity $\bar{\omega}_i$ is updated in order to satisfy the continuity Eq. (5) using the η updated by Eq. (42). Applying the central-upwind method to terms $\partial(Du)/\partial x$ and $\partial(Dv)/\partial y$ in Eq. (5), and applying the second order backward differencing temporal discretization to term $\partial \eta/\partial t$ in Eq. (5), the Eq. (5) is solved as:

$$\begin{aligned} \bar{\omega}_{it}(t + \Delta t) &= \bar{\omega}_{ib}(t + \Delta t) - \Delta \sigma \frac{3 \bar{\eta}_i(t + \Delta t) - 4 \bar{\eta}_i(t) + \bar{\eta}_i(t - \Delta t)}{2 \Delta t} \\ & - \frac{\Delta \sigma}{|V_i|} \sum_{k=1}^5 \frac{A_{ik} n_{x,ik}}{a_{ik}^{\text{in}} + a_{ik}^{\text{out}}} \left[a_{ik}^{\text{in}} ((Du)_{ik}(M_{ik})) + a_{ik}^{\text{out}} ((Du)_i(M_{ik})) \right] \\ & - \frac{\Delta \sigma}{|V_i|} \sum_{k=1}^5 \frac{A_{ik} n_{y,ik}}{a_{ik}^{\text{in}} + a_{ik}^{\text{out}}} \left[a_{ik}^{\text{in}} ((Dv)_{ik}(M_{ik})) + a_{ik}^{\text{out}} ((Dv)_i(M_{ik})) \right] \\ & + \frac{\Delta \sigma}{|V_i|} \sum_{k=1}^5 A_{ik} \frac{a_{ik}^{\text{in}} a_{ik}^{\text{out}}}{a_{ik}^{\text{in}} + a_{ik}^{\text{out}}} \left[\bar{\eta}_{ik}(M_{ik}) - \bar{\eta}_i(M_{jk}) \right]. \end{aligned} \quad (44)$$

where $\bar{\omega}_{it}$ and $\bar{\omega}_{ib}$ are vertical velocities at the top and bottom surfaces of the cell i , respectively. Note that, in the Eq. (44), $Du = Du(t + \Delta t)$, $Dv = Dv(t + \Delta t)$ and $\bar{\eta} = \bar{\eta}(t + \Delta t)$ are computed in Sections 4.1.1 and 4.1.2. Based on the boundary condition $\Omega(x, y, \sigma = 0, t) = 0$, all of the values of $\bar{\omega}_{it}(t^{n+1})$ and $\bar{\omega}_{ib}(t^{n+1})$ can be recursively obtained from (44). At the cell center, $\bar{\omega}_i(t + \Delta t)$ is calculated by

$$\bar{\omega}_i(t + \Delta t) = [\bar{\omega}_{it}(t + \Delta t) + \bar{\omega}_{ib}(t + \Delta t)]/2 \quad (45)$$

4.1.4. Updating the bed profile

The horizontal components of bed-load discharge are calculated by

$$q_{b,x} = \frac{u_0}{\sqrt{u_0^2 + v_0^2}} q_b, \quad q_{b,y} = \frac{v_0}{\sqrt{u_0^2 + v_0^2}} q_b. \quad (46)$$

The bed level in the current model is updated by applying a semi-discrete upwind discretization to the Exner Eq. (12):

$$\begin{aligned} \frac{d \bar{h}_i}{dt} = & - \frac{1}{|T_i|} \sum_{k=1}^3 \ell_{ik} n_{x,ik} \left[\beta_{ik} q_{b,x} (\mathbf{U}_i(M_{ik})) + (1 - \beta_{ik}) q_{b,x} (\mathbf{U}_{ik}(M_{ik})) \right] \\ & - \frac{1}{|T_i|} \sum_{k=1}^3 \ell_{ik} n_{y,ik} \left[\beta_{ik} q_{b,y} (\mathbf{U}_i(M_{ik})) + (1 - \beta_{ik}) q_{b,y} (\mathbf{U}_{ik}(M_{ik})) \right] \end{aligned} \quad (47)$$

where β_{ik} is an upwind coefficient on l_{ik} , which can be estimated by

$$\beta_{ik} = \begin{cases} 0, & \text{if } \frac{1}{2} [u_{0,i}(M_{ik}) + u_{0,ik}(M_{ik})] n_{x,ik} \\ & + \frac{1}{2} [v_{0,i}(M_{ik}) + v_{0,ik}(M_{ik})] n_{y,ik} \geq 0, \\ 1, & \text{otherwise.} \end{cases} \quad (48)$$

4.2. Relaxation step

In this step, we solve the following stiff system

$$\mathbf{U}_t = \mathbf{R}(\mathbf{U}), \quad (49)$$

using an implicit backward Euler method, which gives

$$\bar{\omega}'_i(t + \Delta t) = (\bar{\omega}'_i)^* - \frac{1}{\varepsilon} (\bar{\omega}'_i(t + \Delta t) - \bar{\omega}_i(t + \Delta t)) \quad (50)$$

where $(\bar{\omega}'_i)^*$ is the intermediate values obtained from the propagation step 4.1.

In the small relaxation limit ($\varepsilon \rightarrow 0^+$), this step sets the local equilibrium condition and assigns the auxiliary variables to their relaxed values, i.e., $\bar{\omega}'_i(t + \Delta t) = \bar{\omega}_i(t + \Delta t)$.

4.3. Stability criterion

A fully discrete scheme can be developed from (35) and (47) using a stable ODE solver. In the present study, a total variation diminishing two-stage Runge-Kutta (TVDRK2) solver [9] is used. The time-step size Δt is limited by the following CFL condition:

$$\Delta t^n \leq \min_i \left\{ \min_{k=1,2,3} \left[\frac{r_{ik}}{3 \max(a_{ik}^{\text{in}}, a_{ik}^{\text{out}})} \cdot \frac{\Delta \sigma}{2 \max(b_{ik}^{\text{in}}, b_{ik}^{\text{out}})} \right], \right. \\ \left. \min_{k=4,5} \left[\frac{(\Delta \sigma)^2 D}{2 (v_{0,ik})} \right] \right\}, \quad (51)$$

in which r_{ik} , $k = 1, 2, 3$ are the 3 corresponding altitudes of the prism V_i in the horizontal direction.

5. Model validation

5.1. Quiescent lake over a hump

This test is used to verify the well-balanced property of the present model when a lake is at rest over irregular topography. A hump on a flat bed is first defined as:

$$h(x, y, t = 0) = \max\{0, 2000 - 0.00032[(x - 4200)^2 + (y - 3800)^2], \\ 1000 - [(x - 2900)^2 + (y - 5100)^2]\} \quad (52)$$

The hump is located at the center of a 8000 m × 8000 m computational domain, of which the peak is 2000 m high, and it is completely submerged under a quiescent lake surface which is defined with an initial elevation of 2500 m everywhere. The test is simulated using the parameters: $d = 5$ mm, $s = 2.6$, $p = 0.4$ and $C_B = 8$.

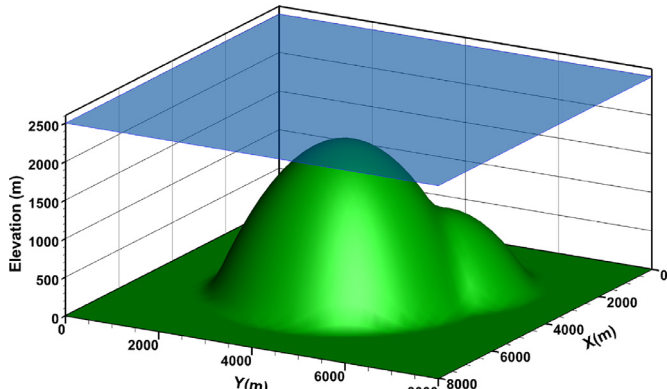


Fig. 2. Simulated quiescent water surface over irregular bottom at $t=50$ s using the proposed well-balanced model.

A constant water surface is observed during the whole simulation process, and the computed velocities are zero over the whole domain. The simulated surface of the quiescent lake at $t=50$ s is shown in Fig. 2. The results show that the proposed model can preserve the well-balanced property.

5.2. 1-D bed erosion with exact solution

The accuracy of the proposed 3-D model is first investigated by a test of dam-break flow over erodible bed in which the bottom shear stress has been neglected in the momentum equation. The exact solution was derived by a process of subsequent wave-field construction demonstrated in [31]. The q_{bx} and q_{by} terms are given by $q_{bx} = A_g u(u^2 + v^2)$ and $q_{by} = A_g v(u^2 + v^2)$ assuming a material characterized by $A_g = 0.01$ and $p = 0.4$. The initial conditions are given by $D = 2.25$ m, $u = 0.2$ m/s and $h = 5.0$ m, for $x < 0$, $D = 1.188686$ m, $u = 2.4321238$ m/s and $h = 5.124685$ m for $x > 0$. A 30 m long domain is discretized by cells with uniform size of 0.01 m in the horizontal direction, and the fluid is discretized into 4 layers in the vertical direction. The computed time is 2 s.

Note that the vertical viscous terms and bed shear stress are not considered in this test.

Fig. 3 shows the comparisons between exact and numerical results for the water surface and bed level. Although some small discrepancies are found at the position of initial discontinuities, a very good agreement between simulated and exact solution is observed. The discontinuities of both shallow water and erodible bed are accurately captured. The results indicate the result of proposed model converges to the exact solution with satisfactory accuracy.

5.3. Dam-break flow over mobile bed

A series of dam-break experiments were conducted by Leal et al. [19] in a 19.2 m long horizontal flume with a width of 0.5 m and a height of 0.7 m. A vertical gate that was originally located in the center of the flume was suddenly removed at $t=0$ s in order to simulate the dam-break. The wave-front travels to the downstream end of the flume in 6 s. Three groups of tests were carried out with respect to the bed types which are fixed bed, sand bed and pumice bed. In the current simulation, a test (Ts.28 in [19]) with sand bed is considered. The sand has a mean particle diameter $d=0.8$ mm with a specific gravity $s=2.65$. The porosity of bed material, p , is determined using the Komura formula [14] modified by Wu and Wang [40]

$$p = 0.13 + \frac{0.21}{(d + 0.002)^{0.21}}.$$

The bed-load coefficient $C_B=8$ is used in this test.

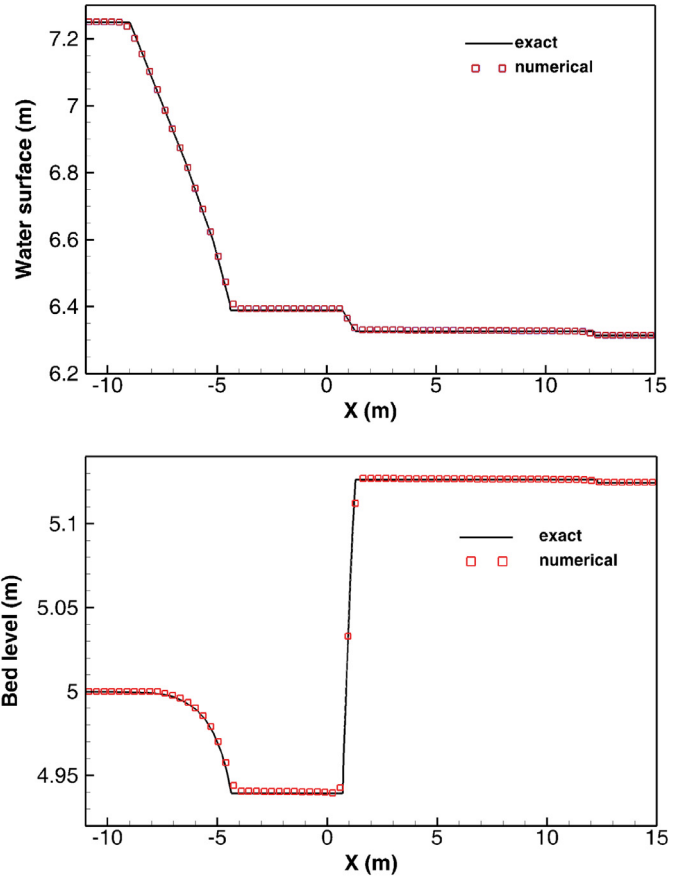


Fig. 3. Comparison between exact and simulated results.

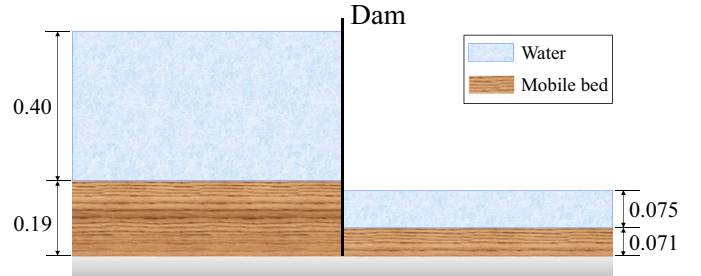


Fig. 4. Initial condition of the dam-break over mobile bed.

At $t=0$ s, a 0.4 m thick flat sand bed is built under a 0.4 m deep quiescent water on the upstream side of the gate, and a 0.071 m thick flat sand bed is built under a 0.075 m deep quiescent water on the downstream side of the gate. The upstream side boundary is defined as a wall boundary condition, and the downstream side boundary is defined as a free outflow boundary condition with a 0.075 m fixed water level. The initial condition is illustrated in Fig. 4.

In the current test, the computational domain is a 20 m \times 0.5 m area which is discretized by 8628 unstructured triangular cells in the horizontal direction and 6 layers in the vertical direction. The horizontal meshes are locally refined in the area near the dam.

Fig. 5 shows the velocity vectors of the dam-break flow at $t=1$ s. Relative high vertical velocity can be observed at the dam-break location ($x=0$ m). An obvious gradient of horizontal velocity at the downstream side of the dam can be seen at around $x=0.6$ m location caused by trans-critical flows, and a hydraulic jump is also observed. This test case emphasizes one of the advantages of the

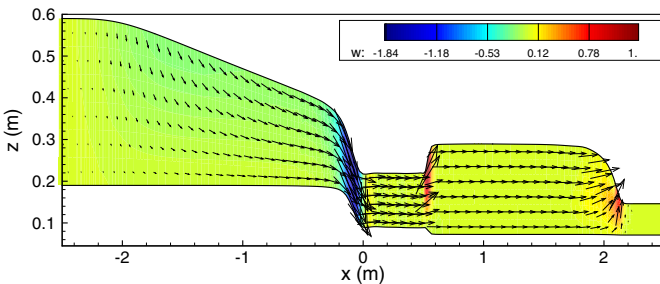


Fig. 5. Velocity vectors of the dam-break flow at $t=1$ s.

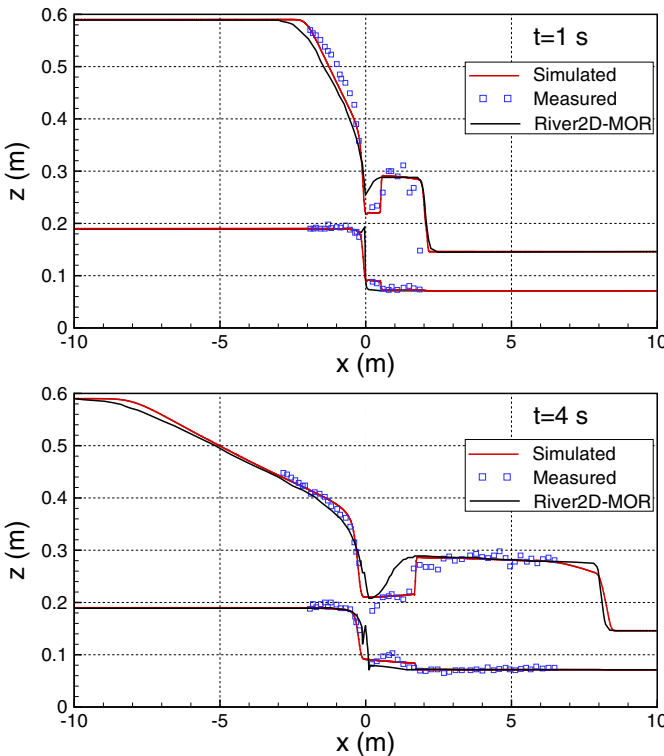


Fig. 6. Simulated and measured results for dam-break flow over mobile bed at $t=1$ s and 4 s.

proposed model which is its ability to capture shock waves over erodible bed.

Fig. 6 shows the comparisons between numerical and experimental results of the current test. It can be observed that the simulated results by the proposed 3-D model show generally good agreement with the experimental measurements at both $t=1$ s and 4 s. The simulated results by the proposed 3-D model are also compared with a published 2-D numerical model (River2D-MOR) reported in [38]. It can be seen that the proposed 3-D model yields better results than the 2-D model on the downstream side near the location of the initial dam. This may be attributed to the fact that, in locations where the vertical velocity cannot be neglected, e.g. the flow at the initial dam location ($x=0$ m) in this test, see Fig. 5, 3-D SW model can yield more accurate prediction of horizontal velocities than a 2-D model. This may lead to more accurate prediction of bed-load transport which is basically driven by horizontal velocities.

5.4. Dam-break flow over mobile bed

The experiments were conducted at the Hydraulics Unit of the Mechanical and Civil Engineering Laboratory in Université

catholique de Louvain, Belgium and the experimental results were published in [33]. The experiment was conducted in a 3.6 m wide flume with a useful length of 27 m. The breached dam was represented by two impervious blocks at about 12 m from upstream end and a 1 m wide gate located between the blocks. The origin of the axes is taken at the gate center. The configuration of experimental setup is shown in Fig. 7. More details of the flume dimensions can be found in [33].

The grey area in Fig. 7 was covered by an 85 mm thick sand layer, which extended over 1.5 m upstream of it and over 9 m downstream of the gate. A flat sand bed without compaction was prepared before the test using uniform coarse sand with a median diameter of $d=1.61$ mm, a specific gravity $s=2.63$, and an initial porosity of $p=0.42$.

The case 1 reported in [33] is used in the current paper to verify the proposed numerical model. In this case, the initial water level in the upstream side of the dam is 0.47 m and the initial water depth is 0 m at the downstream side of the dam. Note that, in order to avoid numerical oscillations caused by dry bed, a 1.0×10^{-4} m water depth is imposed as minimum water depth over the whole computational domain. The temporal water level evolutions were recorded by 8 ultrasonic gauges which were located at: $g_1(0.64$ m, -0.5 m), $g_2(0.64$ m, -0.165 m), $g_3(0.64$ m, 0.165 m), $g_4(0.64$ m, 0.5 m), $g_5(1.94$ m, -0.99 m), $g_6(1.94$ m, -0.33 m), $g_7(1.94$ m, 0.33 m) and $g_8(1.94$ m, 0.99 m). At $t=0$ s, the gate is suddenly removed in order to simulate the dam-break. The experiment was considered to last for 20 s.

The computational domain is discretized by 15,717 triangular cells in horizontal (see Fig. 8) and 6 layers in vertical. The boundary at $x=15.5$ m is set to be free outlet boundary condition, and other boundaries are set to be free-slip wall condition. The bed-load coefficient $C_B=12$ is used in this test.

Fig. 9 shows the temporal evolution of topography under dam-break flow.

Fig. 10 compares the simulated results from the proposed 3-D model and the numerical results estimated by 2D-UCL1 model which were reported in [32,33]. The 2D-UCL1 model uses two-dimensional depth-averaged shallow water equations with MPM formula. It can be observed that, near the location of dam-break ($x=0$ m), the proposed 3-D model yields better results than the 2D-UCL1 model.

Fig. 11 shows the comparisons between simulated and measured water levels at gauges 1 and 6 throughout the dam-break process. Good agreements are observed, and the accuracy of the proposed 3-D model is verified.

5.5. Dam-break flow over mobile bed with a sudden enlargement

This test case is chosen to verify the stability and accuracy of the current model simulating dam-break flows over erodible beds. The laboratory experiment was conducted in the Université catholique de Louvain, Belgium. The experimental results were reported in [10,12,27].

The experiments were conducted in a 6 m long flume, presenting a non-symmetrical sudden widening from 0.25 m to 0.5 m width, located 1 m downstream of the gate which is located at $x=3$ m. The channel width is 0.25 m on the upstream side of $x=4$ m and 0.5 m on the downstream side of $x=4$ m. Ultrasonic gauges and digital imagery equipments are placed and focused on different locations to take the measurements of the water surface and bed profile. The water surface levels are recorded at $P_1(3.75$ m, 0.125 m), $P_2(4.2$ m, 0.125 m), $P_3(4.45$ m, 0.125 m), $P_4(4.95$ m, 0.125 m), $P_5(4.2$ m, 0.375 m), $P_6(4.95$ m, 0.375 m), respectively. In this test, two locations with measured cross-section profiles of bed are chosen to verify the numerical results, which

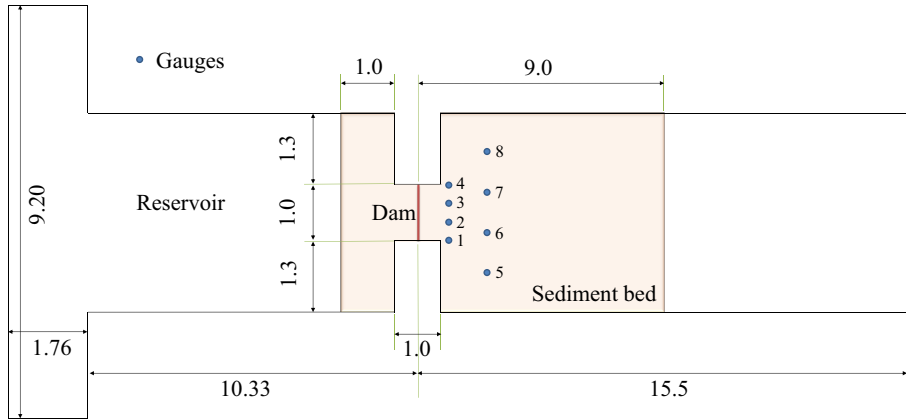


Fig. 7. Plan view of the experimental setup (all the numbers are in meters).

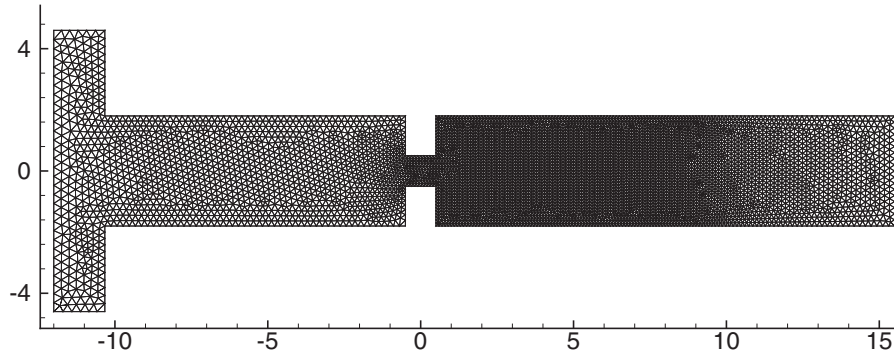


Fig. 8. Horizontal mesh for the computational domain.

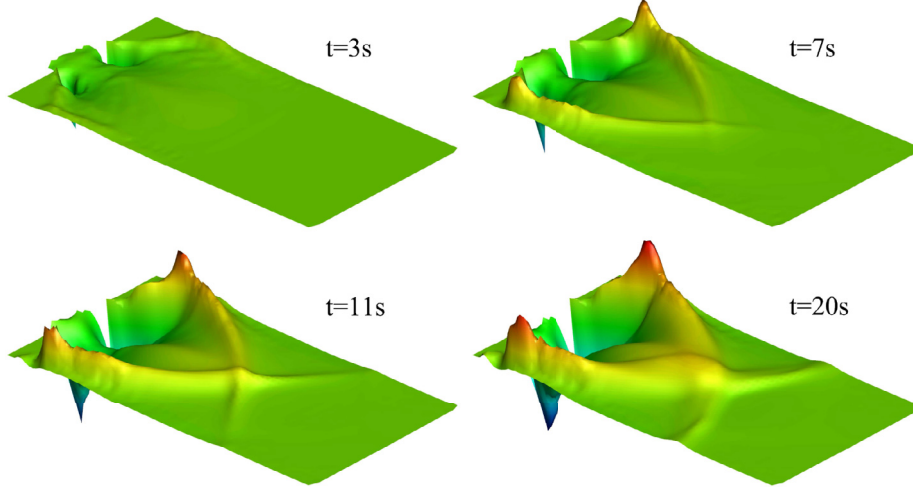


Fig. 9. Temporal evolution of topography.

are at $x=4.1\text{m}$ and $x=4.4\text{m}$, respectively. The configuration of the current test is shown in Fig. 12.

A coarse and almost uniform sand was used as bed material with a median diameter of $d=1.72\text{ mm}$; a specific density of $s=2.63$ and a porosity of $p=0.39$ [2]. At $t=0\text{ s}$, a 0.1 m thick layer of fully saturated sand over the whole flume is setup, and stationary water with a 0.25 m depth is stored in the reservoir on the upstream side of the gate. The gate is suddenly removed at $t=0\text{ s}$, and a dam-break flow with induced bed-load sediment transport travels towards downstream side. A free outflow boundary condition is used at the downstream outlet at $x=6\text{ m}$, and a free-slip

boundary condition is applied at all side walls. The bed-load coefficient $C_B=8$ is used in this test.

The computational domain is discretized by 6389 unstructured triangular cells in the horizontal direction and 5 layers in the vertical direction. Fig. 13 shows the computational grid arrangement at $t=0\text{ s}$.

Fig. 14 shows the simulated horizontal velocity vectors on the water surface. As can be observed, the length of circulating zone is approximately 0.45 m which is close to the measured value in [10]. The simulated flow field is close to the measured one in [10], and different components of the flow structure can be found

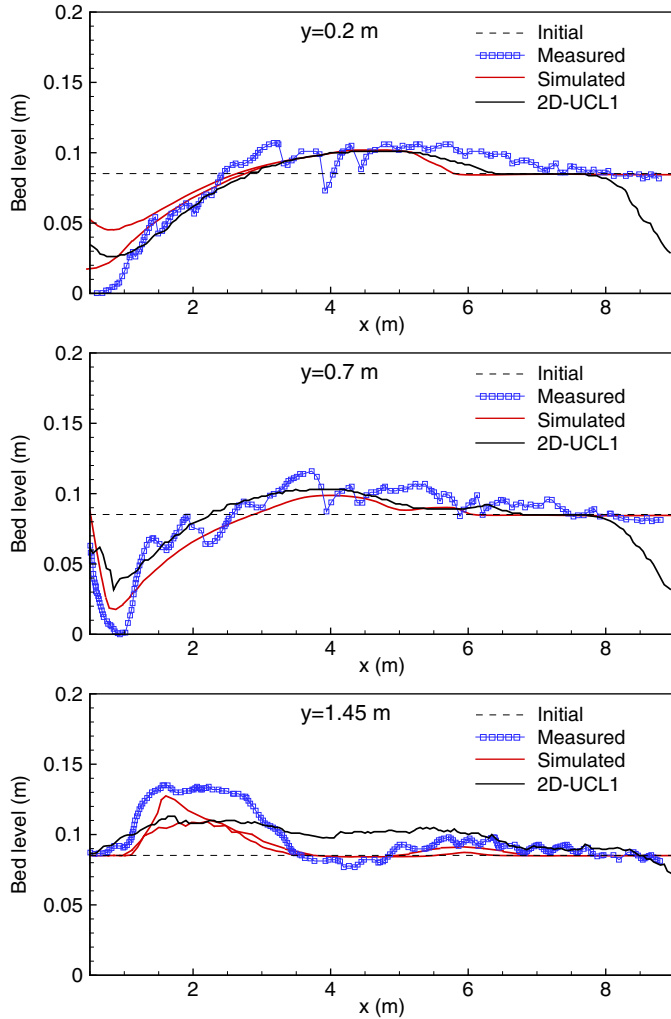


Fig. 10. Comparisons among the measured bed profiles, simulated results by proposed 3-D model and 2D-UCL1 model at $t=20\text{ s}$.

at three indicated regions: in region ①, deviated velocity orientations in the wider reach is observed; in region ②, a recirculation area at the corner forms; and in region ③, an oblique hydraulic jump caused by reflection against the sidewall is observed. Similar features are reported in [10].

Note that, in the proposed model given in sections 2, 3 and 4, the bed shear stress (18) and dimensionless bed shear stress (20) are computed using velocities and discharges in the bottom

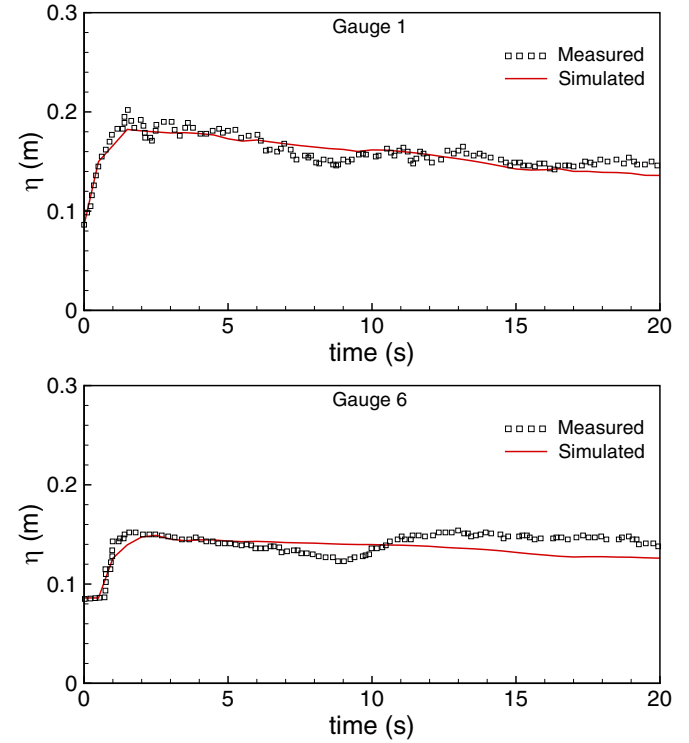


Fig. 11. Simulated and measured water levels at gauge 1 and 6.

layer of computational grids. Such models are denoted by NBV in this numerical test.

If the bed shear stress (18) and dimensionless bed shear stress (20) are computed using depth-averaged velocities and discharges in the proposed model in this study, the model is denoted by DAV in this test.

Fig. 15 shows the comparisons between the simulated and experimentally measured water levels at 6 measured points. An overall good agreement between simulated results and experimental measurements is observed. In Fig. 15, only very small differences are observed between NBV and DAV results.

Fig. 16 shows the comparisons between the simulated and experimentally measured bed profiles at $t=12\text{ s}$ at 2 measured cross-sections which are $x=4.1\text{ m}$ and 4.4 m , respectively. It can be observed that, at $x=4.1\text{ m}$, the NBV model can correctly estimate the scour depth and the position, while the DAV model overestimates the scour depth at around $y=0.25\text{ m}$. At $x=4.4\text{ m}$, the NBV and DAV models can both estimate the correct height and position of the dune, small differences are observed at this cross-section.

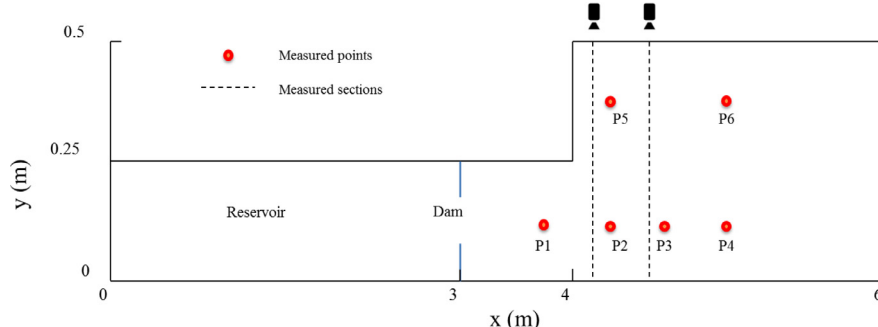


Fig. 12. The configuration of measured points and measured sections of the current test.

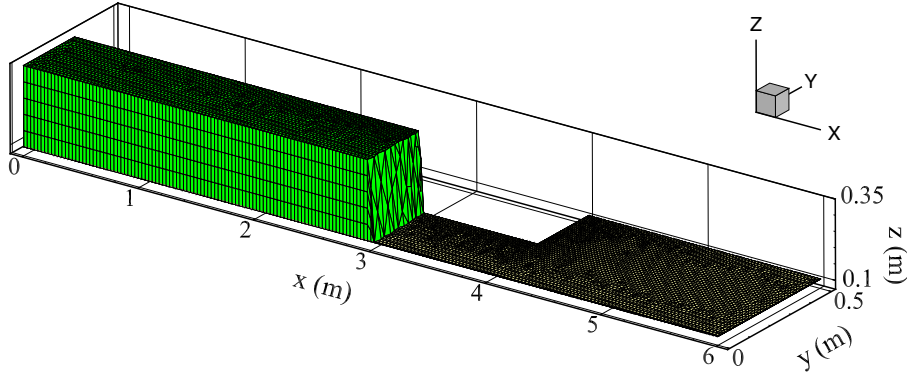


Fig. 13. Arrangement of the 3-D computational cells.

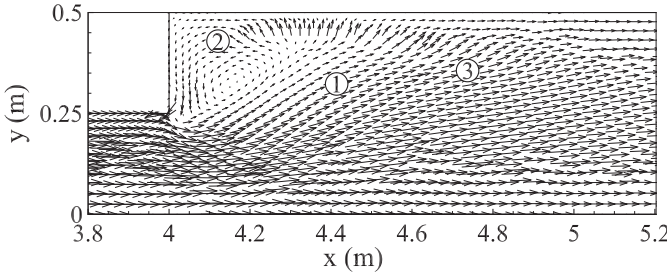


Fig. 14. A comparison between simulated and measured horizontal velocity vectors.

6. Concluding remarks

In the present paper, a 3-D numerical model for shallow water flows with sharp gradients over mobile bed is successfully developed. In hydrodynamic model, the 3-D shallow water equations in σ -coordinates are converted to a hyperbolic form using a relaxation approach, which allows for the use of shock capturing schemes, e.g. central-upwind method. Consequently, the model is able to simulate dam-break flows without numerical instability. A second order “prismatic” central-upwind method is used to estimate the fluxes through interfaces based on explicit finite volume method. The temporal evolution of topography is estimated by an Exner equation consisting of MPM bed-load transport formula which has been widely used in practice. Water and bed levels are updated in a depth-averaged form based on the continu-

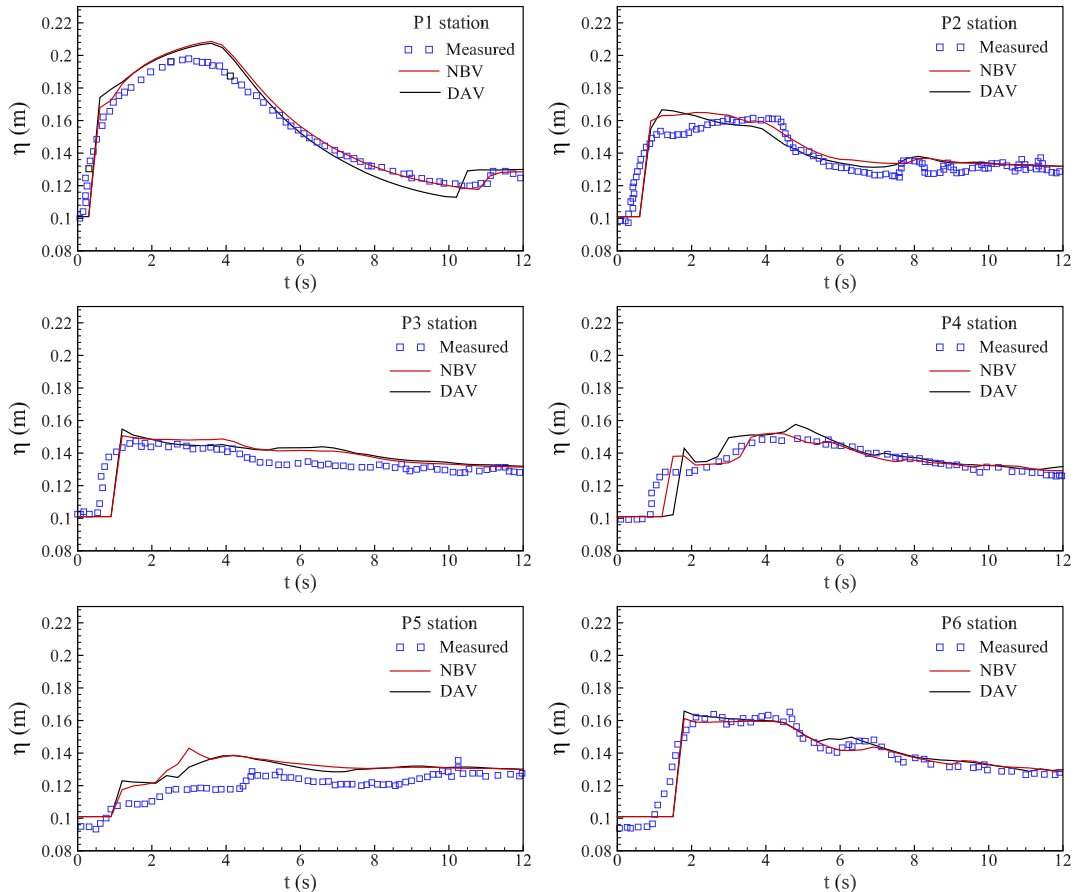


Fig. 15. Simulated and measured water level η at 6 different measured points.

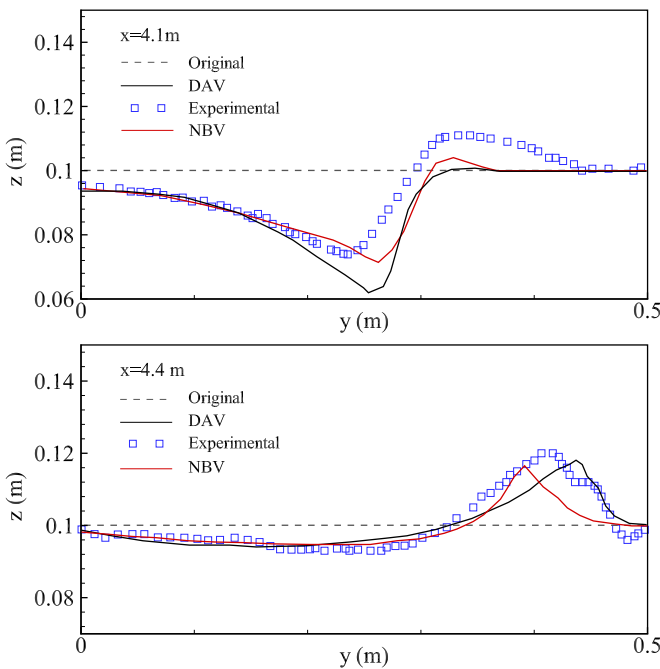


Fig. 16. Simulated and measured bed profiles at different measured sections.

ity equation. The bed-load fluxes in Exner equation are estimated by an upwind method on triangular cells in order to maintain numerical stability. The proposed model has been tested by several laboratory experiments of dam-break flows over mobile beds.

The proposed model can preserve the well-balanced property due to the special discretization of bed-slope source terms, which is verified by 5.1. In the test 5.3 and 5.4, the proposed 3-D model is compared with reported 2-D depth-averaged models; in the test 5.5, the proposed 3-D model using near bed velocities(NBV) is compared with DAV model, the results show that the proposed 3-D model yields better results near the dam-break location due to more accurate prediction of flow field where three-dimensional features can not be neglected.

Acknowledgment

This publication was made possible by NPRP Grant 4-935-2-354 from the [Qatar National Research Fund](#) (a member of the Qatar Foundation). The statements made herein are solely the responsibility of the authors.

References

- [1] Abgrall R, Karni S. Two-layer shallow water system: a relaxation approach. *SIAM J Sci Comput* 2009;31(3):1603–27.
- [2] Becker A, Kaiser D. Ecoulement consécutif à une rupture de barrage dans un canal présentant un élargissement brusque: mesures de la surface libre et de la topographie finale. MSc thesis, Ph.D. thesis, Université catholique de Louvain, Louvain-la-Neuve, Belgium; 2008.
- [3] Blumberg AF, Mellor GL. A coastal ocean numerical model. In: Mathematical modelling of estuarine physics. Springer; 1980. p. 203–19.
- [4] Blumberg AF, Mellor GL. A description of a three-dimensional coastal ocean circulation model. *Three-Dimensional Coastal Ocean Models* 1987;208:1–16.
- [5] Bryson S, Epshteyn Y, Kurganov A, Petrova G. Well-balanced positivity preserving central-upwind scheme on triangular grids for the Saint-Venant system. *M2AN Math Model Numer Anal* 2011;45(3):423–46.
- [6] Canelas R, Murillo J, Ferreira RML. Two-dimensional depth-averaged modelling of dam-break flows over mobile beds. *J Hydraul Res* 2013;51(4):392–407.
- [7] Evangelista S, Altinakar MS, Di Cristo C, Leopardi A. Simulation of dam-break waves on movable beds using a multi-stage centered scheme. *Int J Sediment Res* 2013;28(3):269–84.
- [8] French RH. Open-channel hydraulics; 1985.
- [9] Gottlieb S, Shu CW. Total variation diminishing runge-kutta schemes. *Math Comput Am Math Soc* 1998;67(221):73–85.
- [10] Goutière L, Soares-Frazão S, Zech Y. Dam-break flow on mobile bed in abruptly widening channel: experimental data. *J Hydraul Res* 2011;49(3):367–71.
- [11] Huang W, Cao Z, Carling P, Pender G. Coupled 2d hydrodynamic and sediment transport modeling of megaflood due to glacier dam-break in altai mountains, southern siberia. *J Mt Sci* 2014;11(6):1442–53.
- [12] Iervolino M, Leopoldi A, Soares-Frazão S, Swartzenbroekx C, Zech Y, et al. 2d-h numerical simulation of dam-break flow on mobile bed with sudden enlargement. *River flow 2010 conference*; 2010.
- [13] Jawahar P, Kamath H. A high-resolution procedure for euler and Navier-Stokes computations on unstructured grids. *J Comput Phys* 2000;164(1):165–203.
- [14] Komura S. Discussion of sediment transportation mechanics: introduction and properties of sediment. *J Hydraul Div, ASCE* 1963;89(HY1):263–6.
- [15] Kurganov A, Levy D. Central-upwind schemes for the saint-venant system. *M2AN Math Model Numer Anal* 2002;36:397–425.
- [16] Kurganov A, Noelle S, Petrova G. Semi-discrete central-upwind scheme for hyperbolic conservation laws and Hamilton-Jacobi equations. *J Sci Comput* 2001;23:707–40.
- [17] Kurganov A, Petrova G. Central-upwind schemes on triangular grids for hyperbolic systems of conservation laws. *Numer Methods Partial Diff Equ* 2005;21(3):536–52.
- [18] Kurganov A, Petrova G. A second-order well-balanced positivity preserving central-upwind scheme for the Saint-Venant system. *Commun Math Sci* 2007;5:133–60.
- [19] Leal JGAB, Ferreira RML, Cardoso AH, Bousmar D, Zech Y. Dam-break waves on movable bed. In: *River flow*; 2002. p. 981–90.
- [20] Lesser GR, Roelvink JA, Van Kester JATM, Stelling GS. Development and validation of a three-dimensional morphological model. *Coast Eng* 2004;51(8):883–915.
- [21] Liu X, Infante Sedano JÁ, Mohammadian A. A coupled two-dimensional numerical model for rapidly varying flow, sediment transport and bed morphology. *J Hydraul Res* 2015;1–13.
- [22] Liu X, Infante Sedano JÁ, Mohammadian A. A robust coupled 2-d model for rapidly varying flows over erodible bed using central-upwind method with wetting and drying. *Can J Civ Eng* 2015a;42(8):530–43.
- [23] Liu X, Mohammadian A, Infante Sedano JÁ, Kurganov A. Three-dimensional shallow water system: a relaxation approach. *J Comput Phys* 2017;333:160–79.
- [24] Liu X, Mohammadian A, Kurganov A, Infante Sedano JÁ. Well-balanced central-upwind scheme for a fully coupled shallow water system modeling flows over erodible bed; 2015.
- [25] Meyer-Peter E, Müller R. Formulas for bed-load transport. In: *Proc. 2nd meeting int. assoc. hydraul. struct. res. IAHR*; 1948. p. 39–64.
- [26] Nessyahu H, Tadmor E. Nonoscillatory central differencing for hyperbolic conservation laws. *J Comput Phys* 1990;87(2):408–63.
- [27] Palumbo A, Soares Frazão S, Goutière L, Pianese D, Zech Y, et al. Dam-break flow on mobile bed in a channel with a sudden enlargement. In: *Proc. river flow 2008 conf*; 2008.
- [28] Phillips NA. A coordinate system having some special advantages for numerical forecasting. *J Meteor* 1957;14(2):184–5.
- [29] Rodi W. Turbulence models and their application in hydraulics. CRC Press; 1993.
- [30] Roe PL. Characteristic-based schemes for the euler equations. *Ann Rev Fluid Mech* 1986;18:337–65.
- [31] Serrano-Pacheco A, Murillo J, Garcia-Navarro P. Exact solutions for unsteady 1d shallow water flow over mobile bed. In: *Proc. 6th IAHR symp, Santa Fe, Argentina. River, Coastal and Estuarine Morphodynamics*; 2009. p. 963–7.
- [32] Soares-Frazão S. Dam-break flow on mobile bed benchmark; 2010. http://www.uclouvain.be/cps/ucl/doc/gce/documents/Benchmark_UCL.pdf
- [33] Soares-Frazão S, Canelas R, Cao Z, Cea L, Chaudhry HM, Die Moran A, et al. Dam-break flows over mobile beds: experiments and benchmark tests for numerical models. *J Hydraul Res* 2012;50(4):364–75.
- [34] Soulsby RL. Dynamics of marine sands: a manual for practical applications. Thomas Telford; 1997.
- [35] Soulsby RL, Whitehouse RJS. Threshold of sediment motion in coastal environments. In: Christchurch N, editor. *Pacific coasts and ports '97: proceedings of the 13th Australasian coastal and ocean engineering conference and the 6th Australasian port and harbour conference*, 1; 1997. p. 145–50.
- [36] Swartzenbroekx C, Zech Y, Soares-Frazão S. Two-dimensional two-layer shallow water model for dam break flows with significant bed load transport. *Int J Numer Methods Fluids* 2013;73(5):477–508.
- [37] van Leer B. Towards the ultimate conservative difference scheme. V. A second-order sequel to Godunov's method. *J Comput Phys* 1979;32(1):101–36.
- [38] Vásquez JA, Leal JG. Two-dimensional dambreak simulation over movable beds with an unstructured mesh. In: *River flow, 2*; 2006. p. 1483–91.
- [39] Vásquez J. Two-dimensional finite element river morphology model, Ph.D. thesis. Vancouver, Canada: University of British Columbia; 2005.
- [40] Wu W, Wang SSY. Formulas for sediment porosity and settling velocity. *J Hydraul Eng* 2006;132(8):858–62.
- [41] Xia J, Lin B, Falconer RA, Wang G. Modelling dam-break flows over mobile beds using a 2d coupled approach. *Adv Water Resour* 2010;33(2):171–83.
- [42] Zhang M, Wu WM. A two dimensional hydrodynamic and sediment transport model for dam break based on finite volume method with quadtree grid. *Appl Ocean Res* 2011;33(4):297–308.